Chitosan-Conjugated Dendritic Ag Nanopowders for Photothermal Therapy Applications

Jeong Hoon Byeon*,[†] and Young-Woo Kim*,[‡]

[†]Department of Chemistry, Purdue University, Indiana 47907, United States
[‡]Department of Automotive Engineering, Hoseo University, Asan 336-795, Republic of Korea

Ⓢ *Supporting Information*

ABSTRACT: We report the development of Ag nanodendrites where ultrafine Pd particles served as seeds for the subsequent deposition of Ag on their surfaces. By applying chitosan as both a reductant and a stabilizer, chitosan-conjugated Ag dendritic nanopowders were continuously synthesized using a serial system consisting of a spark discharge, an ultrasound-assisted polyol cell, and a collison atomizer with a heated tubular reactor. The resulting materials were then employed to kill cancerous cells photothermally. A spark discharge between Pd electrodes was employed to vaporize Pd components into a N_2 flow, and finally Pd particles were injected into an ultrasound irradiating Ag polyol cell to initiate Ag deposition on incoming Pd primary particles (~4 nm in lateral dimension). The chitosan-conjugated Ag nanodendrites (~240 nm in lateral dimension) were formed through collison atomization, and the nanodendrites were employed as sensitizers for photothermal cancerous cell killing under near-infrared irradiation in vitro.
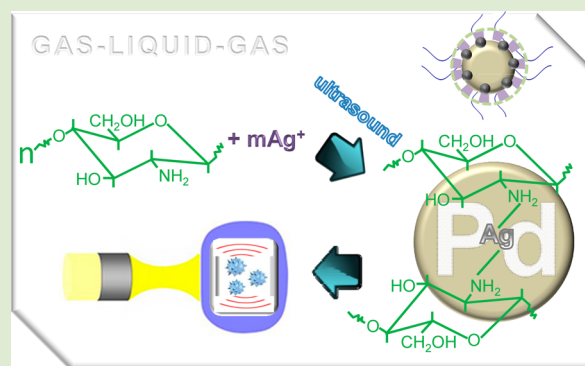
Nanostructures of noble metals, especially the relatively low-cost and highly conductive Ag, have attracted considerable interest in recent years due to their unique electrical, optical, and thermal properties, as well as their potential applications in optoelectronic devices, catalysis, and surface-enhanced Raman scattering (SERS) detection.[1,2] More recently, there has been considerable interest in the synthesis of complex structures composed of nanocrystals, that is, dendritic materials with self-assembled hierarchical and repetitive super-structures, for conductive adhesives, SERS, treatment of cancer, and so on, because such hierarchical materials possess improved properties that originate from their building blocks.[3−5] Regarding their syntheses, seed-assisted growth is probably the most powerful route to complex nanostructures, where preformed seeds of one metal serve as the sites of nucleation and then grow further as another structure. This strategy would direct the heterogeneous nucleation and growth on a seed to follow a conformal or site-selective mode, generating a hierarchical structure.[6]

Photothermal treatment, also known as photothermal ablation or optical hyperthermia, has been actively explored as a minimally invasive approach to cancer therapy.[7] It is a procedure based on localized heating due to light absorption for selective destruction of abnormal cells. In general, near-infrared (NIR) light is preferred for such an application, and the key component of this technique is a photothermal transducer (e.g., organic compounds or materials, metal nanostructures, or carbon-based materials) that can absorb and convert NIR light into heat through a nonradiative

mechanism with high efficiency.[8] When combined with NIR light, all of them are able to generate sufficient heat to raise local temperatures and, thus, kill cancer cells.

Branched (dendritic) or star-shaped Ag nanostructures, consisting of a core and protruding arms, have recently received particular interest due to their unique morphology and optical properties.[9] Owing to the presence of branches as well as their high surface-to-volume ratios, Ag nanodendrites (consisting of several generations of branches with self-similarity) could be effective in photothermal conversion.[10] The synthetic methods used for such materials include electrochemical deposition, surfactant processes, γ- or ultra-sound irradiation, hydrothermal methods, template approaches, and so on.[1] However, most of these wet chemical methods for preparing such dendritic nanostructures are based on the use of surfactants and templates, either for controlling the shape or for stabilization of the formed dendritic Ag nanostructures. However, the addition of reductants or templates may make the synthetic procedure and purification process more complex and further confine biological applications.[4,11−13] Many formulations based on nanomaterial systems exist as colloidal liquids and are generally stable only for short periods of time. Moreover, polymer-incorporated nanomaterial systems are designed to be gradually degradable by hydrolysis, making long-term storage in liquid form not a viable option. One

approach for overcoming these stability limitations is to formulate and store dry powders.[14] Therefore, the exploration of simple synthesis methods with more facile and greener chemical processes for Ag nanodendrites is currently a challenging research area.[2,15−17]

In this project, we assessed the potential use of Ag nanodendrites as photothermal transducers via a hybrid synthesis route to continuously produce the nanodendrites. We conducted the seeded growth of Ag on Pd by introducing an aqueous $AgNO_3$ solution into an aqueous mixture containing both the Pd and the chitosan without any other additives. The use of plasma discharges for nanoscale materials synthesis is a rapidly developing field. In particular, nonthermal plasmas at atmospheric pressure are attractive because of several factors conducive to efficiency.[18] In the liquid reaction, the inserted plasma-produced Pd nanoparticles performed not only as seeds but also as catalysts for reducing Ag(I). Chitosan is a polymer containing many amino groups, which may bond with metallic ions. Hydrated electrons produced during ultrasound irradiation can also reduce Ag(I) to Ag particles of zero valences (Supporting Information). Furthermore, Pd−Ag hybrid structures displayed significantly enhanced photothermal stability compared with pure Ag nanostructures in a previous study.[2] We found that the synthesized Ag nanodendrites exhibited a photothermal activity and biocompatibility in vitro. A spark discharge between Pd electrodes in a N_2 environment was employed to produce ultrafine Pd particles; the particles were injected into an Ag polyol cell under ultrasound irradiation to initiate Ag deposition on the Pd particles (Scheme 1). The cooling rate in the spark is defined

Scheme 1. Conceptual Morphological Evolution of Ag Nanostructures with Increasing Reaction Time During Continuous Pd Particle Injection under Ultrasound Irradiation[a]
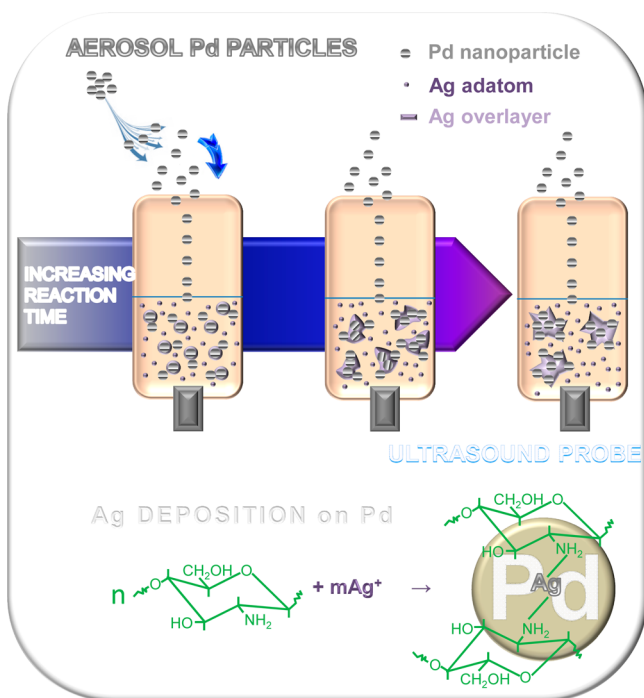
[a]Reaction scheme is also shown as the inset, which shows a reduction of Ag(I) by chitosan molecules.

from a previous study[19] and was −2900 K s^{-1} in the present case. The Pd particles experienced ultrasound when they reached the gas (the Pd particle-laden flow)−liquid (the Ag polyol solution in the cell) interface. The Pd particles in the solution acted as seeds and became kinetically capable of reducing the incoming Ag(I) onto the seeds particles to deposit metallic Ag. When $AgNO_3$ was introduced into an aqueous solution containing chitosan and Pd seeds, the Ag atoms will preferentially nucleate on the surface of a Pd seed via heterogeneous nucleation rather than in the solution phase by themselves via homogeneous nucleation due to a lower activation energy for the former pathway.[4] This approach is most attractive because of its simplicity and versatility. The proposed chemical net reaction on the surface of Pd particles in the polyol cell is also shown in Scheme 1,[20] where they were aerosolized to form nanopowders (Scheme S1) and finally employed as photosensitizers to kill cancerous cells under NIR irradiation.

The gas temperature inside the spark channel was increased beyond a critical value, which was sufficient to sublimate parts of the Pd electrodes.[21] The duration of each spark was very short and the vapors cooled rapidly downstream of the spark. This formed a supersaturation resulting in particle formation through nucleation-condensation. The total number concentration (TNC), geometric mean diameter (GMD), and geometric standard deviation (GSD) of the Pd particles, which were measured using a scanning mobility particle sizer (SMPS, 3936, TSI, U.S.), were 1.24 × 10^8 particles cm^{-3}, 10.8 nm, 1.52, respectively, as shown in Figure 1. The Pd particles
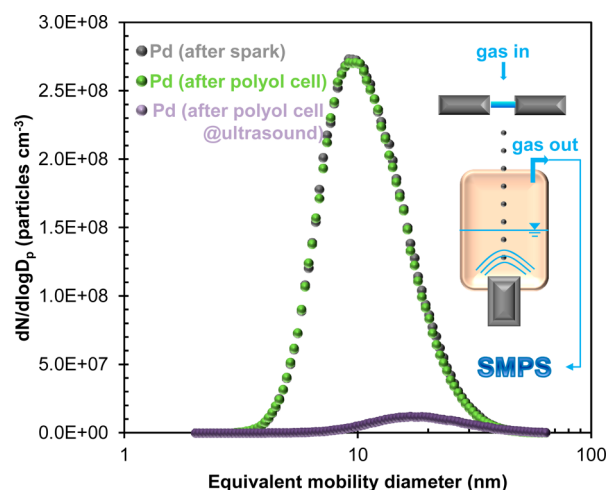

Figure 1. Size distributions of spark-produced Pd particles before and after the polyol cell (with or without ultrasound irradiation). A scheme of the Pd particle collection in the polyol cell is also shown as the inset. Standard deviations are noted in Table SI.

were subsequently injected into an Ag polyol cell to be collected through ultrasound bubble collapsing. We verified the hydrosolization of the aerosol Pd particles by measuring the size distributions with and without the ultrasound irradiation in the gas-phase. Table SI summarizes the size distribution measurements of the Pd particles with and without the ultrasound. The TNC, GMD, and GSD of the Pd particles after the cell in the absence of ultrasound were 1.22 × 10^8 particles cm^{-3}, 10.7 nm, and 1.51, respectively. The analogous data in the presence of ultrasound were 0.06 × 10^8 cm^{-3}, 18.3 nm, and 1.57, respectively. The size distribution in the absence
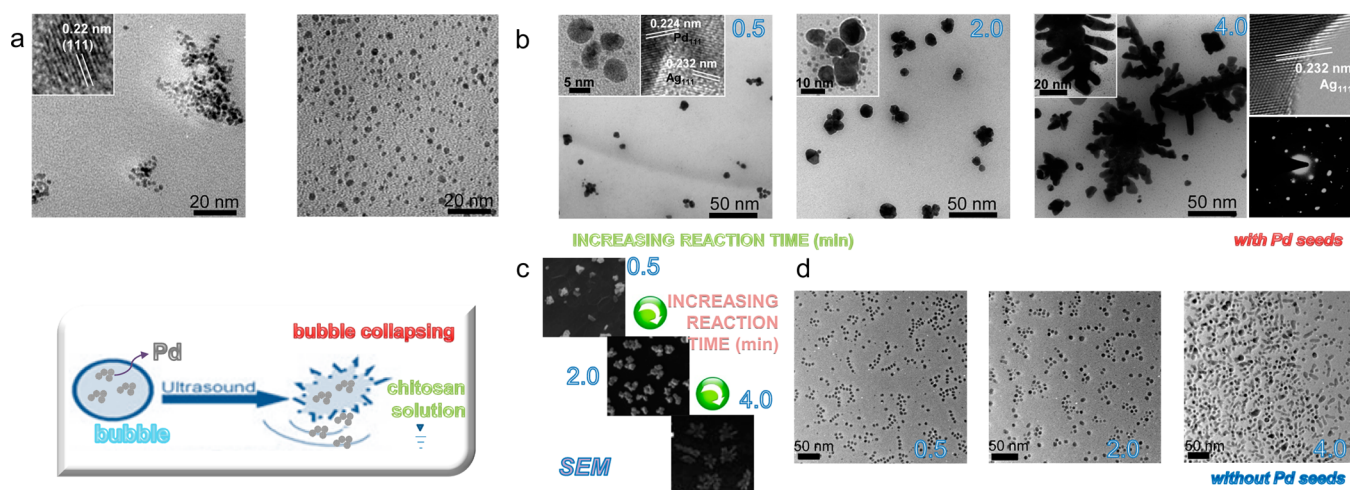
Figure 2. Morphological evolutions of Ag nanostructures with an increasing reaction time range of 0.5−4 min in the polyol cell. (a) Low- and high-magnification TEM images of spark-produced Pd particles before and after injection into the polyol cell. Mechanism of a collection of the Pd particles is also shown as the inset. (b) Low- and high-magnification TEM images of Ag nanostructures with increasing reaction time. A representative electron diffraction pattern of Ag nanodendrites is also shown as the inset. (c) Corresponding SEM images of Ag nanostructures with increasing reaction time. (d) TEM images of Ag nanoparticles with increasing reaction time in the absence of Pd particles.

of ultrasound was nearly identical with the original Pd size distribution, implying that the Pd particles were nearly quantitatively penetrated. In the presence of ultrasound, nearly all Pd particles were collected to be hydrosols in the polyol solution (95.2% collection efficiency), which implies that bubble collapsing by ultrasound irradiation significantly enhances the Pd particle impact on the surface of the polyol solution.

Low- and high-magnification transmission electron microscope (TEM, JEM-3010, JEOL, Japan) images show the morphological evolution of Ag nanostructures with different reaction times, including individual Pd and Ag nanoparticles (Figure 2). A specimen for spark-produced Pd particles was prepared for examination in the TEM by direct electrostatic gas-phase sampling at a sampling flow of 1.0 L min^{-1} and an operating voltage of 5 kV using a Nano Particle Collector (NPC-10, HCT, Korea). A drop of the Pd nanoparticle and Ag nanostructure dispersions was placed on a carbon-coated copper grid, which was allowed to dry before being used for observation following TEM analyses. A morphological evolution study was conducted to obtain a complete view of the Ag dendrite formation process. Products were collected after 0.5, 2, and 4 min of reaction time, and their morphologies were evaluated by TEM. As shown in Figure 2a, the TEM images reveal that the Pd particles (∼16 nm in lateral dimension) were agglomerates of several primary particles, while fragmented Pd particles are shown in the dispersion. As shown in the inset Pd, about 0.22 nm of the lattice fringe of Pd is observed, which can be indexed as the (111) plane of the Pd structure. The fragmentation of Pd agglomerates during the injection into the Ag polyol cell may have originated from the impaction between the Pd agglomerates and the polyol solution surface. Kinetic energy of the Pd agglomerates directed onto the polyol solution with high particle velocity (V_p, eq 1) by ultrasound bubble collapsing (inset of Figure 2a) is 7.26 × 10^{-16} J, which are significantly larger than those (>5 × 10^{-18} J) in previous reports for initiating fragmentation of aerosol agglomerates.[22]

$$V_p = \left(\frac{2P\beta}{\rho_g c_s \pi \alpha^2 X} \right)^{1/2}$$

(1)

where P is the acoustic power of the ultrasound, β is the acoustic energy attenuation coefficient, ρ_g is the gas density, c_s is the sonic velocity in gas, α is the semiangle of the spread of the streaming, and X is the distance from the source.

At the initial stage of the polyol reaction, as shown in Figure 2b, the aggregated nanostructures essentially consisted of two kinds of particles. The one with a darker contrast exhibits the Miller plane (111), 0.224 nm of Pd, whereas the one with a lighter contrast is attributable to the Ag (111), 0.232 nm of lattice fringe. Hence, the process was clearly observed to occur by the initial Ag nucleation at several sites on the continuously incoming Pd followed by growth around these nucleated sites. The increase in particle size with increasing reaction time (i.e., an increase in the Ag content in the bimetallic structures) can be explained by considering the continuous reduction of Ag(I), and as a consequence, the particles grew bigger and anisotropic. The competition for the Ag deposition on different facets may result in anisotropic growth. After 2 min, the agglomerated structures grow larger as ridge-like structures, and further growth leads to dendritic shaped particles (the Ag branches were generated along the ridge-like structures). In the case of Ag dendrites (inset of Figure 2b), the obvious fringes with a ∼0.23 nm interplanar separation correspond to the (111) planes, which indicates that the growth direction of the trunk is along (111). Due to the self-catalytic behavior of Ag, once a nucleus of Ag atoms has been created on the surface of a Pd seed, the reduction of AgNO$_3$ in the following step will preferentially occur at this site rather than other regions on the Pd seed. The Ag nucleus initially grows laterally across the face of a Pd seed and then vertically along the direction perpendicular to the face.[23] This implies that the Ag dendrites grow along a preferential direction since the stem and the side branch have identical crystal orientations; the total dendrite structure is a single crystal. It can be further suggested that the nonequilibrium conditions owing to ultrasound irradiation at the liquid−solid interface provide a driving for the single crystal

dendritic growth.[24,25] It is normally noted that when the shape of the metallic particles is spherical, they are polycrystalline since a slower Ag growth kinetics in the absence of ultrasound might play a certain role in achieving a polygonal transformation during the growth.[26] This would not be a suitable agent for photothermal therapy since spherical Ag particles have a surface plasmon resonance (SPR) band around at 400 nm, not in the NIR region. Whereas, when the particles have a dendritic morphology, they exhibit a single crystalline structure, electron diffraction pattern inset in Figure 2b also indicates that Ag dendrites exhibit a face-centered cubic (fcc) crystalline phase. The SEM results (Figure 2c) are consistent with those observed under TEM investigations. On the other hand, an Ag polyol in the absence of the Pd seeds did not produce dendritic nanostructures under identical operations (Figure 2d), which implies that the Pd seeds performed a critical role in the formation of dendritic Ag nanostructures.

The synthesized Ag nanodendrites were finally aerosolized using a collison atomizer to be formed as nanopowders. Figure S1 shows the size distribution of the aerosolized Ag dendrites. The TNC, GMD, and GSD of the dendrites were 1.49×10^6 particles cm^{-3}, 219.4 nm, 1.79, respectively. Figure S1 also shows a representative TEM image of the aerosolized Ag dendrites. There are no significant changes in morphology after the atomization, which implies that the dendrites have a solid structure to withstand shear stresses during the atomization.

The UV−vis spectrum (330, Perkin-Elmer, U.S., Figure 3) of nanostructures shows that incorporation of Pd with Ag leads to
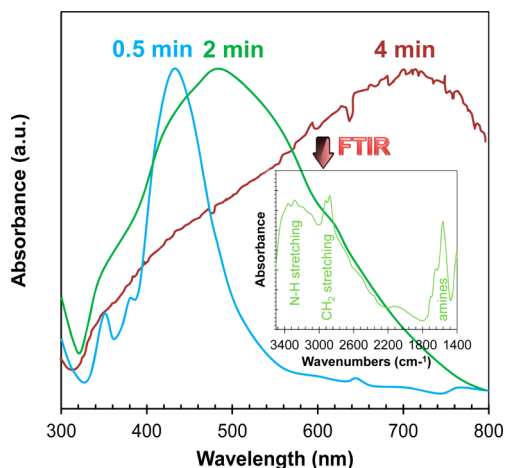

Figure 3. UV−vis spectra of the Ag nanostructures with increasing reaction time ranged 0.5−4 min in the polyol cell. FTIR spectrum of chitosan-conjugated Ag nanodendrites is shown as the inset.

an absorption in the NIR region. The increase in reaction time of Ag polyol in the range of 0.5−4 min leads to a red shift of the absorption plasmon band from 446 to 733 nm, suggesting that the size of the particles increases and the shape changes. The absorption band is significantly broader due to the presence of synthesized Ag nanodendrites, which are shown in Figure 2b. Also, the absorption extends to the NIR red region of 600−900 nm, which is attributed to the in-plane dipole plasmon resonance bands. The SPR absorption of the nanodendrites in the NIR region motivated us to investigate the potential of these materials in photothermal therapy using an NIR laser. Laser radiation within the NIR window is capable of deep tissue penetration due to the high transmission of water

and hemoglobin within these wavelengths, which can be exploited for noninvasive or minimally invasive therapy.[2]

Figure 3 also displays Fourier transform infrared spectra (IFS 66/S, Bruker Optics, Germany) of the aerosolized Ag nanodendrites. N−H and O−H stretching vibrations were characterized by the broad band in the region of 3200−3400 cm^{-1} and bands at 2940 and 2960 cm^{-1} were characteristics of the CH$_2$ bend and CH$_3$ bend, respectively. The conventional N−H bending vibration bands[20] at about 1580 cm^{-1} were shifted to 1570 cm^{-1} along with a decrease in intensity. This suggests the attachment of Ag to nitrogen atoms, which reduces the vibration intensity of the N−H bond due to the molecular weight becoming greater after Ag binding.[27] This implies that the Ag dendrites were passivated with chitosan with bindings.

The crystalline structures of Pd nanoparticles and Ag nanodendrites were further analyzed using X-ray diffraction (XRD, RINT-2100, Rigaku, Japan, inset of Figure S2). The XRD lines appearing at 2θ values of 40.1, 46.7, 68.1, and 82.1° are good matches with the (111), (200), (220), and (311) lattice planes of an fcc Pd (JCPDS file No. 46-1043). The XRD pattern of the Ag dendrites matches well with the Ag fcc structure (JCPDS, No. 04-0783), indicating its high crystallinity. Further, no other diffraction peaks are observed, indicating its high purity, and thus, it is concluded that Ag nanocrystals were successfully prepared in this reaction. This may be because most Pd particles are too small (<4 nm), which is known not to lead to XRD signal.[28] Moreover, the Pd content is very low at the final stage; hence, its signal may be covered by the strong signal of Ag dendrites. Low Pd content and small Pd particle size also imply that much of the crystalline lattice of the Ag dendrite is dominated by the framework of Ag, and thus, the Pd stays on the surface of the Ag dendrites as overlayers rather than forming an alloy with Ag. The ratio of peak intensity (111)/(200) is 4.2 and is higher than the conventional value, namely, 2.5. This indicates the presence of a nonspherical morphology of Ag.[17,29] Moreover, the cell parameter a of the dendrites calculated from the XRD pattern using equations $[\lambda = 2d \sin \theta$ and $1/d = (h^2 + k^2 + l^2)^{1/2}/a]$ is 0.407 nm, which is very close to the reported value of 0.408 nm for Ag nanodendrites.[16] X-ray photoelectron spectroscopy (XPS, AXIS HIS, Kratos Analytical, Japan, inset of Figure S2) spectrum shows that the binding energies at 335.4 and 340.7 eV with a spin−orbit separation of 5.3 eV are attributed to Pd 3d$_{5/2}$ and Pd 3d$_{3/2}$ of metallic Pd and no other peaks due to Pd oxides (336.5−338.0 eV) were observed.[30]

We next examined the ability of the nanodendrites to transfect HeLa cells using plasmid DNA (pDNA) that contain the luciferase and green fluorescent protein (GFP) gene. Zeta potential of chitosan-conjugated Ag nanodendrites was ∼+4.4 mV. Analogous data of the nanodendrites after pDNA complexing was ∼+1.7 mV. The difference in zeta potential between nanodendrites and the pDNA complexes may originate from negatively charged DNA due to the phosphate ions they have loading on the outer surface of the dendrites. The inset in Figure 4 shows the fluorescence of the HeLa cells for the nanodendrites derived from GFP expression, which comfirmed the transfection of Ag dendrite/pDNA complexes. Several dark dots (inset of Figure 4) over the cell further indicate nanodendrite presence inside the cell. In order to investigate the potential of the synthesized nanodendrites as photosensitizers, suspensions of the nanodendrites in agar were irradiated with the NIR ($\lambda = 830$ nm) emitted by a continuous wave laser. This wavelength was chosen since it was relatively
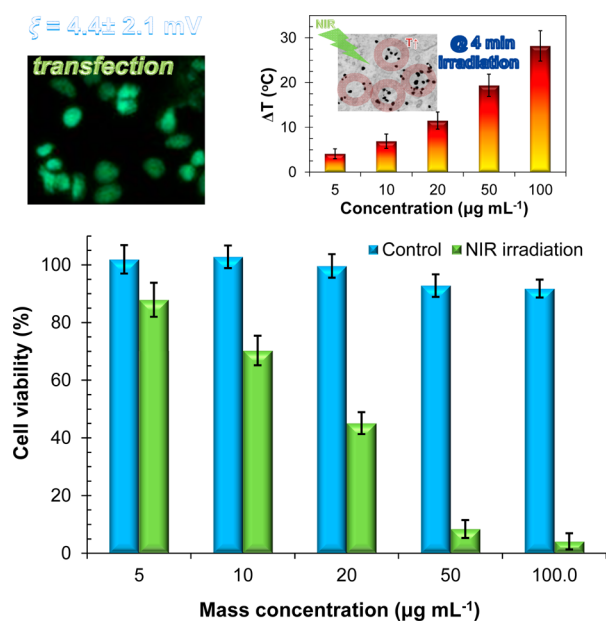
Figure 4. In vitro measurements of photothermal cell killing using chitosan-conjugated Ag nanodendrites with different mass concentrations ranged 5−100 μg mL^{-1}. A fluorescent microscope image for Ag nanodendrites/pDNA complexes is also displayed as the inset. Temperature changes in Ag nanodendrites (5−100 μg mL^{-1} in mass concentration) exposed to a continuous NIR laser fixed at 830 nm for 4 min is shown as another inset. A representative microscope image (another inset) shows black dots inside the cell, further confirms the intracellular transfection of the nanodendrites.

close to the peak value of the Ag nanodendrites determined by UV−vis spectroscopy (Figure 3). The agar phantom was used to mimic physiological conditions.

We observed a localized heating of the sample in the region exposed to laser radiation by an IR thermometer (42545, Extech, U.S.). Figure 4 also shows the change in temperature (ΔT) of the agar gels containing the Ag nanodendrites (5−100 μg mL^{-1}). In comparison, the temperature of the sample in the absence of the dendrites was increased by only 0.6 °C. The maximum value of ΔT (28.2 °C) was observed at the highest concentration (100 μg mL^{-1}). The results indicated that the nanodendrites could absorb NIR and rapidly convert the light energy into environmental heat. The equation can be solved analytically in the steady-state regime, yielding a maximum temperature located at the surface of the nanodendrite:[31]

$$\Delta T(D_n) = \frac{V_n P_{abs}}{2\pi k_0 D_n} \qquad (2)$$

where V_n is the volume of the nanodendrite, k_0 is the thermal conductivity of the surrounding material, and P_{abs} is the local light-induced heating of the nanodendrite. In order to confirm the feasibility of the nanodendrites in photothermal therapy, adenosine triphosphate (ATP) assay was further employed. It is well-known that most cancer cells depend on glycolysis for ATP generation.[32] It was found that in the presence of the nanodendrites in the culture medium, the laser radiation depleted ATP production, which implies that irreversible thermo/chemical modifications of a variety of cell constituents are induced. Figure 4 also shows the cells after incubation for 48 h with the as-prepared Ag nanodendrites (i.e., in the absence of NIR light) at different concentrations ranging from 5 to 100 μg mL^{-1} did not show significant decrease in ATP production,

indicating that they were nontoxic due to the passivation with chitosan and better biocompatibility than that in a previous report.[10] Nevertheless, the highest increase in temperature at 100 μg mL^{-1} may not be suitable in actual applications because of a thermal shock, which implies that the dose of the nanodendrites should be optimized to enhance photothermal activity without a significant damage of other cells.

We developed for the first time an aerosol-based synthesis to produce chitosan-conjugated dendritic Ag nanopowders in a continuous manner via a serial system consisting of a spark discharge reactor, an ultrasound-assisted polyol cell, and a collison atomizer with a heated tubular reactor, and we further tested their photothermal activities to kill HeLa cells under NIR irradation. Simple methods, nontoxic chemicals, and continuous production make this synthesis suitable for efficient photothermal therapy. We believe this provides new perspectives and useful information for low-cost and more efficient photosensitizers for biomedical applications.

■ ASSOCIATED CONTENT

Ⓢ Supporting Information

The schematic diagram of aerosol-based synthesis of dendritic Ag nanopowders, mechanism of Ag(I) reduction, size distribution and TEM image of chitosan-conjugated Ag nanodendrites, XRD spectra of the Pd particles and Ag dendrites, and XPS spectrum of the Pd nanoparticles. This material is available free of charge via the Internet at http://pubs.acs.org.

■ AUTHOR INFORMATION

Corresponding Authors
*Tel.: +1-765-494-5499. E-mail: jbyeon@purdue.edu.
*Tel.: +82-41-540-5819. E-mail: ywkim@hoseo.edu.

Notes
The authors declare no competing financial interest.

■ REFERENCES

(1) Zhang, G.; Sun, S.; Banis, M. N.; Li, R.; Cai, M.; Sun, X. *Cryst. Growth Des.* **2011**, *11*, 2493−2499.
(2) Huang, X.; Tang, S.; Liu, B.; Ren, B.; Zheng, N. *Adv. Mater.* **2011**, *23*, 3420−3425.
(3) Byeon, J. H.; Kim, Y.-W. *Nanoscale* **2012**, *4*, 6726−6729.
(4) Qin, X.; Miao, Z.; Fang, Y.; Zhang, D.; Ma, J.; Zhang, L.; Chen, Q.; Shao, X. *Langmuir* **2012**, *28*, 5218−5226.
(5) Chen, X.; Cui, C.-H.; Guo, Z.; Liu, J.-H.; Huang, X.-J.; Yu, S.-H. *Small* **2011**, *7*, 858−863.
(6) Zeng, J.; Zhu, C.; Tao, J.; Jin, M.; Zhang, H.; Li, Z.-Y.; Zhu, Y.; Xia, Y. *Angew. Chem., Int. Ed.* **2012**, *51*, 2354−2358.
(7) Wang, Y.; Black, K. C. L.; Luehmann, H.; Li, W.; Zhang, Y.; Cai, X.; Wan, D.; Liu, S.-Y.; Li, M.; Kim, P.; Li, Z.-Y.; Wang, L. V.; Liu, Y.; Xia, Y. *ACS Nano* **2013**, *7*, 2068−2077.
(8) Jain, P. K.; Huang, X.; El-Sayed, I. H.; El-Sayed, M. A. *Acc. Chem. Res.* **2008**, *41*, 1578−1586.
(9) Ren, W.; Guo, S.; Dong, S.; Wang, E. *J. Phys. Chem. C* **2011**, *115*, 10315−10320.
(10) Hu, K.-W.; Huang, C.-C.; Hwu, J.-R.; Su, W.-C.; Shieh, D.-B.; Yeh, C.-S. *Chem.—Eur. J.* **2008**, *14*, 2956−2964.
(11) Sun, L.; Liu, A.; Tao, X.; Zhao, Y. *J. Mater. Sci.* **2011**, *46*, 839−845.
(12) Noroozi, M.; Zakaria, A.; Moksin, M. M.; Wahab, Z. A.; Abedini, A. *Int. J. Mol. Sci.* **2012**, *13*, 8086−8096.
(13) Zhang, X.; Ji, R.; Wang, L.; Yu, L.; Wang, J.; Geng, B.; Wang, G. *CrystEngComm* **2013**, *15*, 1173−1178.
(14) Byeon, J. H.; Roberts, J. T. *ACS Appl. Mater. Interfaces* **2012**, *4*, 2693−2698.

(15) Johnson, L.; Thielemans, W.; Walsh, D. A. *J. Mater. Chem.* **2010**, *20*, 1737−1743.

(16) Rashid, M. H.; Mandal, T. K. *J. Phys. Chem. C* **2007**, *111*, 16750−16760.

(17) Wang, L.; Li, H.; Tian, J.; Sun, X. *ACS Appl. Mater. Interfaces* **2010**, *2*, 2987−2991.

(18) Ostrikov, K.; Neyts, E. C.; Meyyappan, M. *Adv. Phys.* **2013**, *62*, 113−224.

(19) Byeon, J. H.; Kim, J.-W. *Appl. Phys. Lett.* **2010**, *96*, 153102.

(20) Huang, N. M.; Radiman, S.; Lim, H. N.; Khiew, P. S.; Chiu, W. S.; Lee, K. H.; Syahida, A.; Hashim, R.; Chia, C. H. *Chem. Eng. J.* **2009**, *155*, 499−507.

(21) Byeon, J. H.; Park, J. H.; Hwang, J. *J. Aerosol Sci.* **2008**, *39*, 888−896.

(22) Rothenbacher, S.; Messerer, A.; Kasper, G. *Part. Fibre Toxicol.* **2008**, *5*, 9.

(23) Wang, D.; Li, T.; Liu, Y.; Huang, J.; You, T. *Cryst. Growth Des.* **2009**, *9*, 4351−4355.

(24) Wang, X.-K.; Shao, L.; Guo, W.-L.; Wang, J.-G.; Zhu, Y.-P.; Wang, C. *Ultrason. Sonochem.* **2009**, *16*, 747−751.

(25) Wang, F.; Lai, Y.; Zhao, B.; Hu, X.; Zhang, D.; Hu, K. *Chem. Commun.* **2010**, *46*, 3782−3784.

(26) Byeon, J. H.; Kim, Y.-W. *Ultrason. Sonochem.* **2012**, *19*, 209−215.

(27) Venkatesham, M.; Ayodhya, D.; Madhusudhan, A.; Babu, N. V.; Veerabhadram, G. *Appl. Nanosci.* **2013**, DOI: 10.1007/s13024-012-0180-y.

(28) Huang, J.; Vongehr, S.; Tang, S.; Lu, H.; Meng, X. *J. Phys. Chem. C* **2010**, *114*, 15005−15010.

(29) Sivasubramanian, R.; Sangaranarayanan, M. V. *CrystEngComm* **2013**, *15*, 2052−2056.

(30) Xiao, J.; Xie, Y.; Tang, R.; Chen, M.; Tian, X. *Adv. Mater.* **2001**, *13*, 1887−1891.

(31) Neumann, O.; Urban, A. S.; Day, J.; Lal, S.; Nordlander, P.; Halas, N. J. *ACS Nano* **2013**, *7*, 42−49.

(32) Huang, H.; Liu, N.; Guo, H.; Liao, S.; Li, X.; Yang, C.; Liu, S.; Song, W.; Liu, C.; Guan, L.; Li, B.; Xu, L.; Zhang, C.; Wang, X.; Dou, Q. P.; Liu, J. *PLoS One* **2012**, *7*, e49062.